The effect of noncondensables on buoyancy-thermocapillary convection of volatile fluids in confined geometries

Tongran Qin[a], Roman O. Grigoriev[b]

[a]*George W. Woodruff School of Mechanical Engineering, Georgia Institute of Technology, Atlanta, GA 30332-0405, USA*
[b]*School of Physics, Georgia Institute of Technology, Atlanta, GA 30332-0430, USA*

Abstract

Recent experimental studies have shown that buoyancy-thermocapillary convection in a layer of volatile liquid subjected to a horizontal temperature gradient is strongly affected by the presence of noncondensable gases, such as air. Specifically, it was found that removing most of the air from a sealed cavity containing the liquid and its vapors significantly alters the flow structure and, in particular, suppresses transitions between the different convection patterns found at atmospheric conditions. Yet, at the same time, the concentration of noncondensables has almost no effect on the flow speeds in the liquid layer, at least for the parameter range studied in the experiments. To understand these results, we have formulated and numerically implemented a detailed model that accounts for mass and heat transport in both phases as well as the phase change at the interface. The predictions of this model, which assumes that the gas phase is dominated by either noncondensables or the vapor, agree well with experiments in both limits. Furthermore, we find that noncondensables have a large effect on the flow at concentrations even as low as 1%, i.e., values much lower than those achieved in experiment.

Keywords: buoyancy-thermocapillary convection, buoyancy-Marangoni convection, free surface flow, two phase flow, noncondensable gas, flow instability, thermocapillarity, numerical simulation

1. Introduction

Convection in volatile fluids with a free surface due to a combination of thermocapillary stresses and buoyancy has been studied extensively due to applications in thermal management. In particular, devices such as thermosyphons, heat pipes, and heat spreaders, which use phase change to enhance thermal transport, are typically sealed, with most of the noncondensables (such as air), which can impede phase change, removed [1]. However, air tends to dissolve in liquids and be adsorbed into solids, so removing it completely is usually not feasible. Hence, the liquid film almost always remains in contact with a mixture of its own vapor and some air.

The fundamental studies on which the design of such devices is based, however, often do not distinguish between different compositions of the gas phase (e.g., varying amounts of air in the system). The vast majority of experimental studies was performed in geometries that are not sealed and hence contain air at atmospheric pressure. Yet, as a recent experimental study of convection in a volatile silicone oil (hexamethyldisiloxane) by Li *et al.* [2] showed, noncondensables can play an important role, so the results in one limit cannot be simply extrapolated to the other. Theoretical studies, on the other hand, tend to use a piecemeal approach based on breaking up the entire system into an "evaporator," a "condenser," and an "adiabatic region" in-between [3, 4], often without checking whether such partitioning is justified or attempting to correlate the transport processes in the three regions.

The effect of noncondensables on filmwise condensation of vapors in simple geometries (thin liquid layers of condensate on flat or cylindrical surfaces) is reasonably well understood. In particular, in the absence of noncondensables, the heat transfer coefficient is controlled by the thickness of the draining film [5]. Condensation is reduced dramatically in the presence of noncondensables. In this case thermal resistance is typically dominated by the diffusion of vapors through a layer of noncondensables that accumulate next to the condensate film, which can be described using boundary layer theory for both free convection [6] and forced convection [7]. For instance, very small amounts of noncondensables – mass fractions as small as 0.5% – will halve the condensation rate, and the corresponding heat transfer coefficient, for steam condensation [6].

The vast majority of theoretical studies of buoyancy-thermocapillary convection use one-sided models which describe transport in the liquid, but not the gas phase and ignore phase change, with both phase change and transport in the gas phase indirectly incorporated through boundary conditions at the liquid-vapor interface [8, 9, 10, 11, 12]. The predictions of such models are mostly consistent with experimental studies of volatile and nonvolatile fluids at ambient (atmospheric) conditions [8, 13, 14, 15, 2] which find that, for dynamic Bond number of order unity, the flow in the liquid layer transitions from a steady unicellular pattern (featuring a single large convection roll) to a steady multicellular pattern (featuring multiple steady convection rolls) to an oscillatory pattern (featuring multiple unsteady convection rolls) as the applied temperature gradient (and hence the Marangoni number) is increased.

Indeed, at atmospheric conditions phase change is strongly

suppressed due to diffusion of vapors through air, so phase change plays a relatively minor role. However, upon closer examination, one finds that one-sided models fail to predict some important features of the problem. We have recently introduced a comprehensive two-sided model [16, 17, 18] of buoyancy-thermocapillary convection in confined fluids which provides a detailed description of momentum, heat and mass transport in both the liquid and the gas phase as well as phase change at the interface *in the entire system.* This model shows that at atmospheric conditions Newton's Law of Cooling, which serves as a foundation for all the one-sided models, completely breaks down [18]. Furthermore, one finds, rather counter-intuitively, that there are regions of evaporation (condensation) next to the cold (hot) end wall of the cavity containing the fluid [17].

In comparison, very few studies have been performed in the (near) absence of noncondensables. One notable exception is the study of Li *et al.* [2], who performed experiments for a volatile silicone oil. They found that the transitions between different convection patterns were suppressed when the concentration of noncondensables was reduced. In particular, only the steady unicellular regime is observed over the entire range of imposed temperature gradients at the lowest average air concentration investigated (14%). Interestingly, the experiments also show that, at small imposed temperature gradients, the flow structure and speeds remain essentially the same as the air concentration decreases from 96% (ambient conditions) to 14%, which corresponds to a reduction by more than two orders of magnitude in the partial pressure of air.

There are at present no theoretical models that are capable of explaining these experimental observations. The theoretical studies [19, 20, 21, 22, 23] available to date employ extremely restrictive assumptions and/or use a very crude description of one of the two phases. Our own two-sided model [18], which treats the gas phase as pure vapor, correctly predicts the suppression of transitions between convection patterns. However, it also predicts that thermocapillary stresses essentially vanish and the flow speed decreases substantially, which is not consistent with experimental observations. The high flow velocities found in experiment imply that thermocapillary stresses remain significant, which suggests that the presence of noncondensables in the gas phase, even at rather low concentrations, has a profound effect on the flow and has to be accounted for.

Hence, to better understand the effect of noncondensables on heat and mass transport in volatile fluids in confined and sealed geometries, our two-sided model [16, 17, 18] was further generalized to describe situations where the gas phase is dominated by vapor, but still contains a small amount of noncondensables [24]. The model is described in detail in Section 2. The results of the numerical investigations of this model are presented, analyzed, and compared with experimental observations in Section 3 and our summary and conclusions are presented in Section 4.

2. Mathematical Model

2.1. Governing Equations

We describe transport in both the liquid and the gas phase using a generalization of the pure-vapor model [18]. The present model is very similar to the one introduced in Ref. [17] (which describes transport at atmospheric conditions when the gas phase is a binary mixture dominated by air), but now the gas phase is dominated by vapor, rather than air. Both phases are considered incompressible and the momentum transport in the bulk is described by the Navier-Stokes equation

$$\rho \left(\partial_t \mathbf{u} + \mathbf{u} \cdot \nabla \mathbf{u} \right) = -\nabla p + \mu \nabla^2 \mathbf{u} + \rho \left(T, c_a \right) \mathbf{g} \tag{1}$$

where p is the fluid pressure, ρ and μ are the fluid's density and viscosity, respectively, c_a is the concentration of air, and $\mathbf{g}$ is the gravitational acceleration. (The air is noncondensable, so $c_a = 0$ in the liquid phase.) Following standard practice, we use the Boussinesq approximation, retaining the temperature and composition dependence only in the last term to represent the buoyancy force. In the liquid phase

$$\rho_l = \rho_l^* [1 - \beta_l (T - T^*)], \tag{2}$$

where ρ_l^* is the reference density at the reference temperature T^* and $\beta_l = -(\partial \rho_l / \partial T) / \rho_l$ is the coefficient of thermal expansion. Here and below, subscripts l, g, v, a, and i denote properties of the liquid and gas phase, vapor and air component, and the liquid-vapor interface, respectively. In the gas phase

$$\rho_g = \rho_a + \rho_v, \tag{3}$$

where both vapor ($n = v$) and air ($n = a$) are considered to be ideal gases

$$p_n = \rho_n \bar{R}_n T, \tag{4}$$

$\bar{R}_n = R / M_n$, R is the universal gas constant, and M_n is the molar mass. The total gas pressure is the sum of partial pressures

$$p_g = p_a + p_v. \tag{5}$$

On the left-hand-side of (1) the density is considered constant for each phase. We set it equal to the spatial average of $\rho(T, c_a)$.

To ensure local mass conservation of air, which is the less abundant component in the gas phase, we describe mass transport using the advection-diffusion equation for its density

$$\partial_t \rho_a + \mathbf{u} \cdot \nabla \rho_a = D \nabla^2 \rho_a, \tag{6}$$

where D is the binary diffusion coefficient of one component in the other. For a volatile fluid in confined geometry, the external temperature gradient causes both evaporation and condensation, with the net mass of the fluid being globally conserved

$$\int_{\text{liquid}} \rho_l dV + \int_{\text{gas}} \rho_v dV = m_{l+v}, \tag{7}$$

where m_{l+v} is the total mass of liquid and vapor. The total pressure in gas phase is $p_g = p + p_o$, where the (constant) pressure offset p_o is

$$p_o = \left[\int_{\text{gas}} \frac{dV}{\bar{R}_v T} \right]^{-1} \left[m_{l+v} - \int_{\text{liquid}} \rho_l dV - \int_{\text{gas}} \frac{p dV}{\bar{R}_v T} \right]. \tag{8}$$

The concentrations (or, more precisely, the molar fractions) of the two components can be computed from the equation of state using the partial pressures

$$c_n = p_n / p_g. \tag{9}$$

2

Finally, the transport of heat is also described using an advection-diffusion equation

$$\partial_t T + \mathbf{u} \cdot \nabla T = \alpha \nabla^2 T, \tag{10}$$

where $\alpha = k/(\rho c_p)$ is the thermal diffusivity, k is the thermal conductivity, and c_p is the heat capacity, of the fluid.

The transport equations (1), (6) and (10) in the gas phase essentially represent the leading order of the Chapman-Enskog expansion [25], which is valid when the temperatures of the two components are the same. As argued by Hamel [26], when the masses of the two components are substantially different (for instance, for hexamethyldisiloxane $M_v \approx 162$ g/mol^{-1}, while for air $M_a \approx 29$ g/mol^{-1}), a more accurate description would require the introduction of two different temperatures $T_a \neq T_v$ and some modifications to all the transport equations. Most importantly, the Navier-Stokes equation in the dilute approximation is written for the dominant component, rather than for the mixture, and includes an additional term for the cross-collision momentum transport. However, for the problem considered here the cross-collision frequency characterized by the dimensionless parameter Cr is high ($Cr \gg 1$ for $c_a \gg 10^{-9}$), and in this limit [26] Hamel's generalized model effectively reduces to the Chapman-Enskog description.

2.2. Boundary Conditions

The system of coupled evolution equations for the velocity, pressure, temperature, and density fields should be solved in a self-consistent manner, subject to the boundary conditions describing the balance of momentum, heat, and mass fluxes. The phase change at the free surface can be described using Kinetic Theory [27]. As we have shown previously [18], the choice of the phase change model has a negligible effect on the results. The mass flux across the interface is given by [28]

$$J = \frac{2\lambda}{2 - \lambda} \rho_v \sqrt{\frac{\bar{R}_v T_i}{2\pi}} \left[\frac{p_l - p_g}{\rho_l \bar{R}_v T_i} + \frac{\mathcal{L}}{\bar{R}_v T_i} \frac{T_i - T_s}{T_s} \right], \tag{11}$$

where λ is the accommodation coefficient (for nonpolar liquids $\lambda \approx 1$ [29, 30]), $\mathcal{L}$ is the latent heat, and subscript s denotes saturation values for the vapor. The dependence of the local saturation temperature on the partial pressure of vapor is described using the Antoine equation for phase equilibrium

$$\ln p_v = A_v - \frac{B_v}{C_v + T_s}, \tag{12}$$

where A_v, B_v, and C_v are empirical coefficients. The Antoine equation generalizes the Clausius-Clapeyron equation and is valid over a wider range of temperatures and pressures.

The mass flux balance for the vapor is given by

$$J = -D\,\hat{\mathbf{n}} \cdot \nabla \rho_v + \rho_v\,\hat{\mathbf{n}} \cdot (\mathbf{u}_g - \mathbf{u}_i), \tag{13}$$

where the first term represents the diffusion component, the second term represents the advection component (referred to as the "convection component" by Wang et al. [31]), and $\mathbf{u}_i$ is the velocity of the interface. Since air is noncondensable, its mass flux across the interface is zero:

$$0 = -D\,\hat{\mathbf{n}} \cdot \nabla \rho_a + \rho_a\,\hat{\mathbf{n}} \cdot (\mathbf{u}_g - \mathbf{u}_i). \tag{14}$$
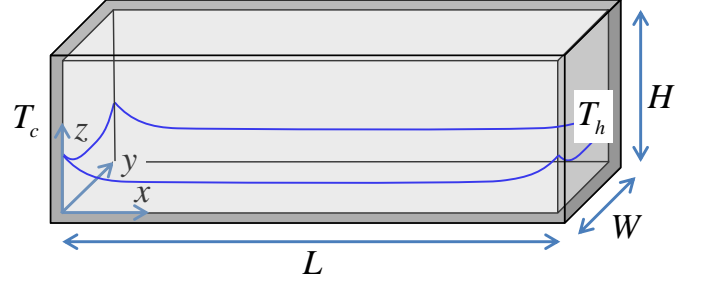

Figure 1: The test cell containing the liquid and air/vapor mixture. Gravity is pointing in the negative z direction. The shape of the contact line reflects the curvature of the free surface.

The mass diffusivity D is a function of pressure and temperature

$$D = D^* \frac{p^*}{p} \left(\frac{T}{T^*} \right)^{3/2}, \tag{15}$$

where D^* is the diffusion coefficient at reference temperature T^* and pressure p^*. For binary diffusion, the concentration gradients of vapor and air have the same absolute value but opposite directions, which yields the relation between the density gradients of vapor and air

$$\frac{\hat{\mathbf{n}} \cdot \nabla \rho_v}{M_v} + \frac{\hat{\mathbf{n}} \cdot \nabla \rho_a}{M_a} = -\frac{p_g}{RT_i^2} \left(\hat{\mathbf{n}} \cdot \nabla T_g \right). \tag{16}$$

The heat flux balance is given by

$$\mathcal{L}J = \hat{\mathbf{n}} \cdot k_g \nabla T_g - \hat{\mathbf{n}} \cdot k_l \nabla T_l. \tag{17}$$

The advective contribution to the heat flux can be ignored on both sides. In the gas phase conduction is the dominant contribution (due to the large value of thermal diffusivity α_g), while on the liquid side $\hat{\mathbf{n}} \cdot (\mathbf{u}_l - \mathbf{u}_i)$ is negligibly small. Indeed,

$$\hat{\mathbf{n}} \cdot (\mathbf{u}_l - \mathbf{u}_i) = \frac{J}{\rho_l} \tag{18}$$

and, since the liquid density is much greater than that of the gas, the left-hand-side of (18) is very small compared with $\hat{\mathbf{n}} \cdot (\mathbf{u}_g - \mathbf{u}_i)$ and can be set to zero.

The remaining boundary conditions for $\mathbf{u}$ and T at the liquid-vapor interface are standard: the temperature is continuous

$$T_l = T_i = T_v \tag{19}$$

as are the tangential velocity components

$$(1 - \hat{\mathbf{n}} \cdot \hat{\mathbf{n}})(\mathbf{u}_l - \mathbf{u}_g) = 0. \tag{20}$$

The stress balance

$$(\Sigma_l - \Sigma_g) \cdot \hat{\mathbf{n}} = \hat{\mathbf{n}} \kappa \sigma - \gamma \nabla_s T_i \tag{21}$$

incorporates both the viscous drag between the two phases and the thermocapillary effect. Here $\Sigma = \mu \left[\nabla \mathbf{u} - (\nabla \mathbf{u})^T \right] - p$ is the stress tensor, κ is the interfacial curvature, $\nabla_s = (1 - \hat{\mathbf{n}} \cdot \hat{\mathbf{n}}) \nabla$ is the surface gradient, and $\gamma = -\partial \sigma / \partial T$ is the temperature coefficient of surface tension.

We further assume that the fluid is contained in a rectangular test cell with inner dimensions $L \times W \times H$ (cf. Fig. 1)

and thin walls of thickness δ_w and conductivity k_w. The left wall is cooled with constant temperature T_c imposed on the outside, while the right wall is heated with constant temperature $T_h > T_c$ imposed on the outside. Since the walls are thin, one-dimensional conduction is assumed, yielding the following boundary conditions on the inside of the side walls:

$$T|_{x=0} = T_c + \frac{k_n}{k_w}\delta_w\,\hat{\mathbf{n}}\cdot\nabla T, \qquad (22)$$

$$T|_{x=L} = T_h + \frac{k_n}{k_w}\delta_w\,\hat{\mathbf{n}}\cdot\nabla T, \qquad (23)$$

where $n = g$ ($n = l$) above (below) the contact line.

Since in most experiments side walls are nearly adiabatic, heat flux through the top, bottom, front, and back walls is ignored. Standard no-slip boundary conditions $\mathbf{u} = 0$ for the velocity and no-flux boundary conditions

$$\hat{\mathbf{n}}\cdot\nabla\rho_a = 0 \qquad (24)$$

for the density of air are imposed on all the walls. The pressure boundary condition follows from (1)

$$\hat{\mathbf{n}}\cdot\nabla p = \rho(T)\,\hat{\mathbf{n}}\cdot\mathbf{g}, \qquad (25)$$

when the inertial and viscous stresses are neglected.

3. Results and Discussion

The model described above has been implemented numerically by adapting an open-source general-purpose CFD package OpenFOAM [32] to solve the governing equations in both 2D and 3D geometries. Newton iteration is used to solve the system of equations (4), (11), (12), (13), (14), (16), and (17) for the mass flux J, the interfacial temperature T_i, the saturation temperature T_s, the normal component of the gas velocity at the interface $\hat{\mathbf{n}}\cdot(\mathbf{u}_g - \mathbf{u}_i)$, the density of the vapor ρ_v, and the normal component of the density gradients of the two components of the gas, $\hat{\mathbf{n}}\cdot\nabla\rho_v$ and $\hat{\mathbf{n}}\cdot\nabla\rho_a$. After this the bulk transport equations (1), (6), and (10) are solved for $\mathbf{u}$, ρ_a, and T, and the process is iterated until convergence. More details concerning the implementation are available in Ref. [17].

In this section, we will use the computational model to investigate the buoyancy-thermocapillary flow of a volatile silicone oil (hexamethyldisiloxane) confined in a sealed rectangular test cell used in the experimental study of Li *et al.* [2]. The properties of the working fluid are summarized in Table 1. A layer of liquid of average thickness $d_l = 2.5$ mm is confined in the test cell with the inner dimensions $L \times H \times W = 48.5$ mm $\times 10$ mm $\times 10$ mm (*cf.* Fig. 1), below a layer of gas, which is a mixture of vapor and air, held around the vapor pressure. The walls of the test cell are made of quartz (fused silica) with thermal conductivity $k_w = 1.4$ W/m-K and have thickness $\delta_w = 1.25$ mm. Though the silicone oil wets quartz well, we set the contact angle $\theta = 50°$ here to avoid numerical instabilities. This has a minor effect on the shape of the free surface everywhere except very near the contact lines; moreover, previous studies [17] show that the influence of the contact angle on the flow pattern is relatively weak. We verified that the weak dependence

	liquid	vapor	air
μ (kg/(m·s))	5.27×10^{-4}	5.84×10^{-6}	1.81×10^{-5}
ρ (kg/m^3)	765.5	0.27	1.20
β (1/K)	1.32×10^{-3}	3.41×10^{-3}	3.41×10^{-3}
k (W/(m·K))	0.110	0.011	0.026
α (m^2/s)	7.49×10^{-8}	2.80×10^{-5}	2.12×10^{-5}
Pr	9.19	0.77	0.71
D (m^2/s)	-	1.46×10^{-4}	5.84×10^{-6}
σ (N/m)	1.58×10^{-2}		
γ (N/(m·K))	8.9×10^{-5}		
$\mathcal{L}$ (J/kg)	2.25×10^{5}		

Table 1: Material properties of pure components at the reference temperature $T_0 = 293$ K [33, 34]. For the gas phase, the weighted average of the two components (based on the average air concentration $\bar{c}_a$) is used. The coefficients A_v, B_v, and C_v for the Antoine's equation were taken from Ref. [35].

on θ and also on the wall thickness δ_w persists over the entire range of the average concentration of air $\bar{c}_a$.

While the numerical model can describe the flows in both 2D and 3D systems, the results presented here are obtained exclusively for 2D flows (ignoring variation in the y-direction), since 3D simulations require significant computational resources and comparison of 2D and 3D results for the same system under air at atmospheric conditions shows that 3D effects are rather small [17]. The 2D system corresponds to the central vertical (x-z) plane of the cavity.

Initially, the fluid is assumed stationary with uniform temperature $T_0 = (T_c + T_h)/2$ (= 293 K in all cases), the liquid layer is of uniform thickness (such that the liquid-vapor interface is flat), and the gas layer is a uniform mixture of vapor and air. The partial pressure of vapor is set equal to the saturation pressure at T_0, $p_v = p_s(T_0) \approx 4.1$ kPa, calculated from (12). The partial pressure of air was used as a control parameter, which determines the net mass of air in the cavity. Our initial simulations showed that the effect of temperature dependence of material parameters on the heat and mass transport is quite small. Therefore, all final results presented below were obtained using the values at the reference temperature.

As the system evolves towards an asymptotic state, the flow develops in both phases, the interface distorts to accommodate the assigned contact angle at the walls, and the gradients in the temperature and vapor concentration are established. The simulations are first performed on a coarse hexahedral mesh (initially all cells are cubic with a dimension of 0.5 mm), since the initial transient state is of secondary interest. Once the transient dynamics have died down, the simulations are continued after the mesh is refined in several steps, until the results become mesh-independent.

The experimental study of Li *et al.* [2] investigated the impact of two parameters – the average concentration $\bar{c}_a$ of air and the imposed temperature difference ΔT – on the convection pattern arising in the liquid layer. Our previous studies of the limiting cases (atmospheric conditions [17] and pure vapor [18]) identified thermocapillary stresses as the main driving force controlling the flow in the liquid layer. These stresses are

determined by the interfacial temperature profile which, in turn, depends on the concentration field in the gas phase. We will therefore also look at how $\bar{c}_a$ and ΔT affect the mass transport in the gas phase and the associated concentration field.

3.1. Solutions in the bulk

In order to investigate the effect of noncondensables on the the flow, we performed numerical simulations for ΔT varying between 0.01 K and 30 K and $\bar{c}_a$ varying between 0 (pure vapor) and 0.96 (atmospheric pressure). We used the numerical model described in Ref. [17] in the cases where the gas phase is dominated by air (here $\bar{c}_a \geq 0.85$), the numerical model described in Section 2 in the cases where the gas phase is dominated by vapor (here $0 < \bar{c}_a \leq 0.16$), and the numerical model described in Ref. [18] in the absence of air ($\bar{c}_a = 0$).

3.1.1. Flow field

The dependence of the flow on the imposed temperature gradient was discussed in many other studies, including our own [17], so here we will concentrate on the dependence of the flow on the concentration of noncondensables at a fixed $\Delta T = 10$ K. Fig. 2 shows the streamlines of the flow in both the liquid and the gas phases. At atmospheric conditions, $\bar{c}_a = 0.96$ (or 96% air), we find an oscillatory multicellular flow (OMC) with convection rolls covering the entire liquid layer. The amplitude of oscillation, however, is extremely small, so the flow can effectively be considered steady.

As the average air concentration is lowered, the convection rolls gradually weaken and disappear, starting near the cold end wall. This can be seen already at $\bar{c}_a = 0.85$, where a steady multicellular flow (SMC) is found. When the concentration of air is lowered to 16% ($\bar{c}_a = 0.16$), all of the convection rolls disappear except for two, one near each end wall. In the central region we find a horizontal return flow which has the same profile in any vertical cross section (the corresponding velocity field in the liquid layer is known analytically [36, 17]). This flow is referred to as a steady unicellular flow (SUF). As $\bar{c}_a$ is reduced to 8% or below, the horizontal flow speed becomes nonuniform, with a pronounced minimum forming around $x \approx 38$ mm. The flow at these low, but nonzero values of $\bar{c}_a$ is qualitatively similar to that found under pure vapor ($\bar{c}_a = 0$) [18].

The flow in the gas phase is not directly observable in experiment, so numerical simulation is, at present, the only way to describe the transport of vapors. Two features of this flow are worth mentioning. First of all, as $\bar{c}_a$ is reduced, the global flow structure changes gradually but qualitatively. At (near-) atmospheric conditions ($\bar{c}_a \geq 0.85$) we find a return flow with the gas (mostly noncondensables) flowing from the hot to the cold wall along the free surface and in the opposite direction along the top of the cavity, with almost all streamlines closed. In the (near-) absence of air ($\bar{c}_a \leq 0.04$) the flow is unidirectional, with the gas (mostly vapor) flowing from the hot to the cold end wall. At intermediate concentrations ($\bar{c}_a = 0.08$ and 0.16) the velocity field exhibits features of both types of flows: there is a region of recirculation (closed streamlines) near the top of the cavity, but most of the streamlines originate and terminate on the interface, as one would expect for a gas mixture

$\bar{c}_a = 0$ (0% air)

$\bar{c}_a = 0.04$ (4% air)

$\bar{c}_a = 0.08$ (8% air)

$\bar{c}_a = 0.16$ (16% air)

$\bar{c}_a = 0.85$ (85% air)
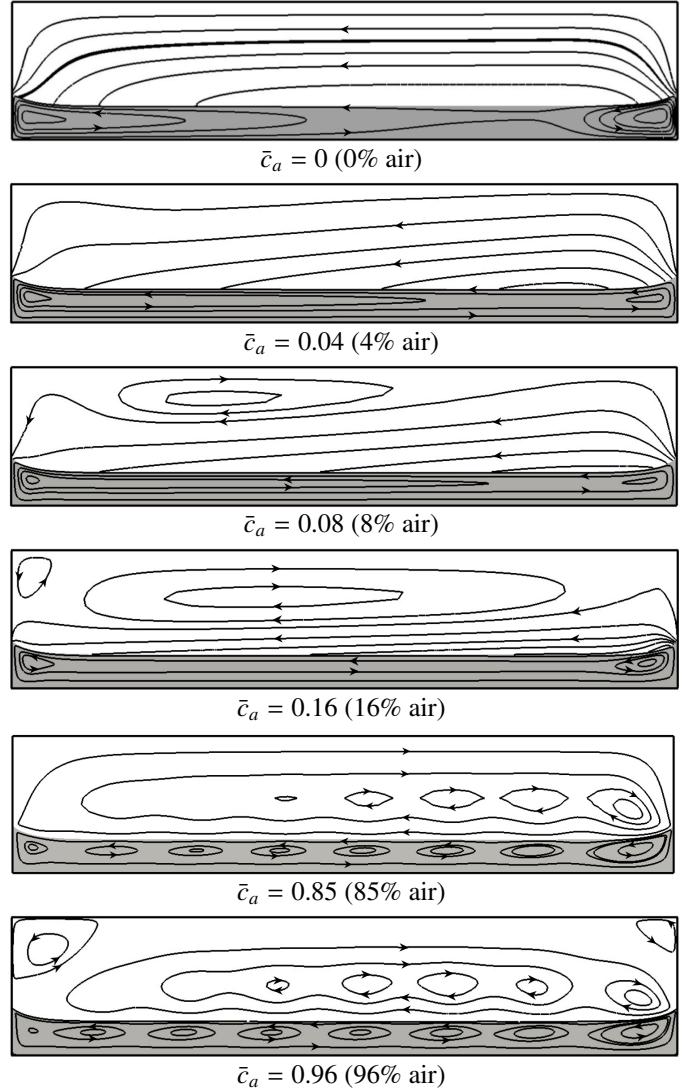
$\bar{c}_a = 0.96$ (96% air)

Figure 2: Streamlines of the flow (solid lines) at different average concentrations of air. The temperature difference is $\Delta T = 10$ K. The arrows indicate the direction of the flow. Here and below, the gray (white) background indicates the liquid (gas) phase.

dominated by vapor. Second, at (near-) atmospheric conditions we also find local convection rolls in the gas phase located directly above the respective convection rolls in the liquid phase for $\bar{c}_a$. This reflects the dominant role of interfacial processes in destabilization of the uniform return flow and the emergence of convection pattern. Correspondingly, there are no convection rolls in the gas phase when steady unicellular flow is found in the liquid layer.

3.1.2. Temperature field

Figure 3 shows the temperature fields corresponding to the flow fields from Fig. 2. The temperature field in the gas phase is qualitatively similar for all $\bar{c}_a$, but in the liquid it depends noticeably on $\bar{c}_a$. At intermediate values of $\bar{c}_a$ (here 0.08 and 0.16) the temperature in the central portion of the liquid layer has a simple profile consistent with the analytical solution in
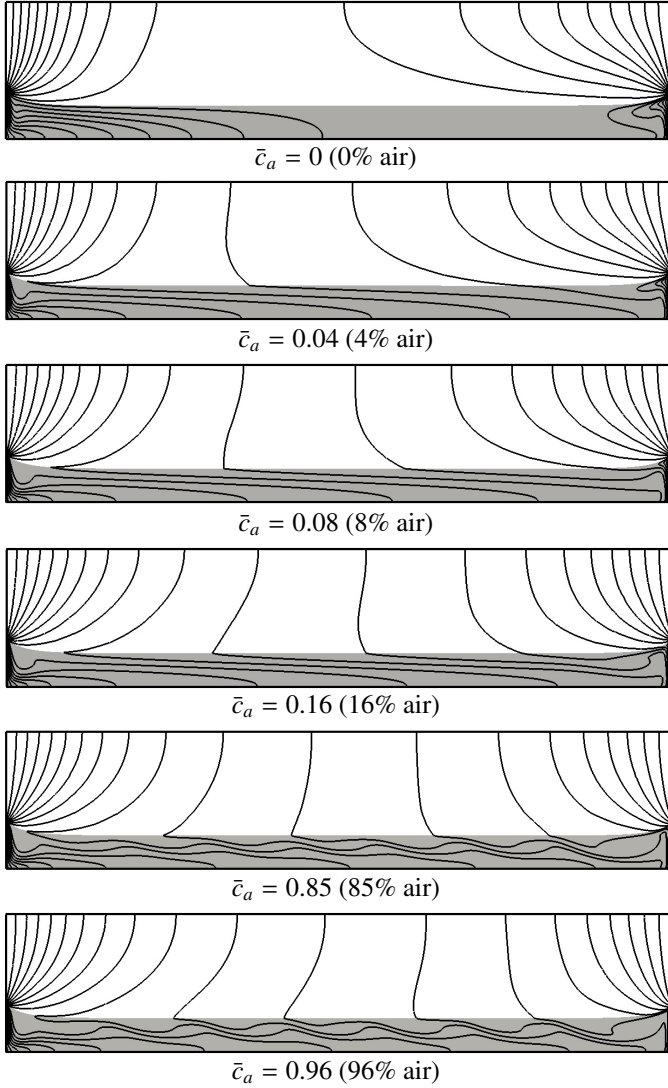
Figure 3: The temperature field inside the cavity at different average concentrations of air. The temperature difference is $\Delta T = 10$ K and the difference between adjacent isotherms (solid lines) is 0.5 K. The temperature increases from left to right.

Figure 4: Air concentration c_a in the gas phase for $\Delta T = 10$ K and different $\bar{c}_a$. The interval between adjacent level sets and the total variation for c_a are different. In the gas phase, darker shade indicates higher air concentration, while in the liquid phase, the concentration field is not defined.

the SUF regime [36, 17]

$$T = \tau x + \hat{T}(z), \tag{26}$$

where $\tau = \partial_x T_i$ is the (nearly constant) interfacial temperature gradient and the vertical profile $\hat{T}(z)$ is a polynomial function of the depth. A qualitatively similar state is also found at (near-) atmospheric conditions and $\Delta T \lesssim 2$ K (not shown). For $\bar{c}_a \geq 0.85$ the temperature field displays a noticeable modulation about the profile (26) caused by the advection of heat by the flow. For $\bar{c}_a \lesssim 0.08$ the temperature in the central portion of the liquid layer also deviates from the profile (26), but there is no periodic modulation due to the absence of convection rolls. Instead, the gradient τ varies, decreasing with x.

Some qualitative features of the temperature field, on the other hand, are independent of $\bar{c}_a$. For instance, the isotherms show strong clustering in the liquid phase near both end walls, indicating the formation of thermal boundary layers. In con-
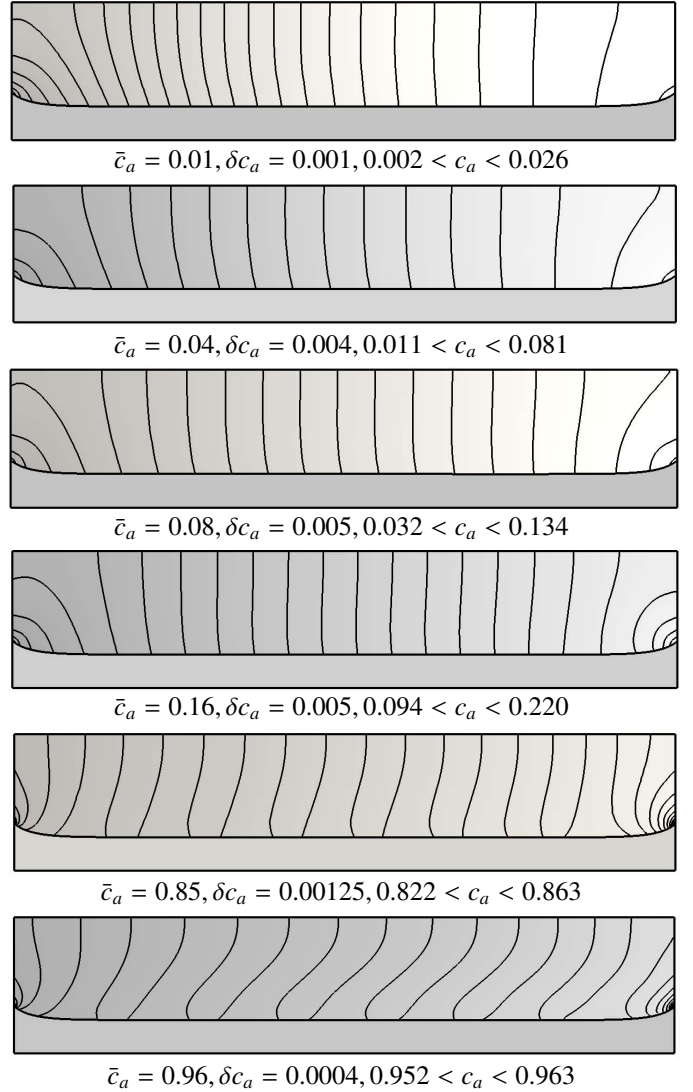
trast, no thermal boundary layers form near the end walls in the gas phase. Instead, the temperature field appears to be insensitive to the fluid flow and is dominated by heat conduction, which appears odd, given that thermal conductivity k_g of the gas is considerably smaller than thermal conductivity k_l of the liquid. However, in steady state the temperature field is instead controlled by the thermal diffusivity α, which is much higher in the gas than in the liquid (see Table 1) due to the vastly different densities, which explains why conduction dominates.

3.1.3. Concentration field

While the liquid phase is a simple fluid, the gas phase is a binary fluid, except for the pure vapor case $\bar{c}_a = 0$. The concentration field in the gas phase for different $\bar{c}_a$ is shown in Fig. 4. The concentration of air is a decreasing function of x for all $\bar{c}_a$, which is consistent with the air being swept by the flow of vapor towards the cold end wall. For $\bar{c}_a \geq 0.85$ we find c_a to
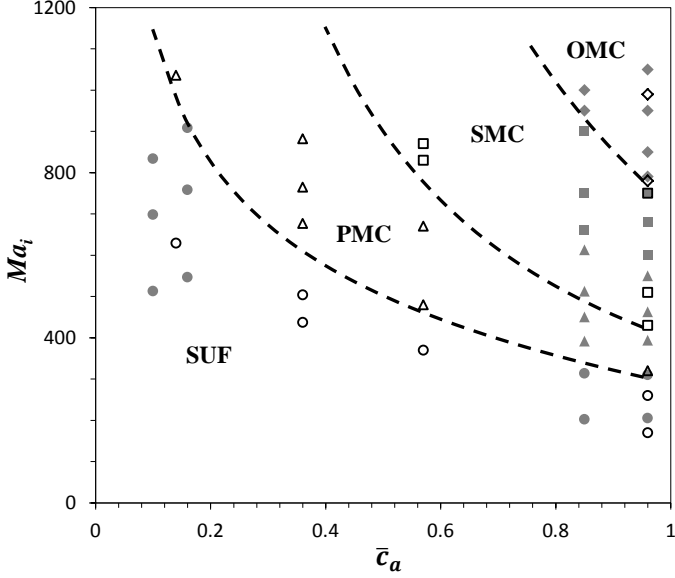
Figure 5: Flow regimes: SUF (○), PMC (△), SMC (□), and OMC (◇). Open symbols correspond to experimental results of Li *et al.* and filled symbols – to numerical results from this study. Dashed lines are sketches of the boundaries between different regimes (based on the experimental results).

vary in a small range about the average. The horizontal concentration profile is linear near the top of the cavity, while near the interface we find significant spatial modulation about the linear profile caused by advection of the gas mixture by the convective flow.

As $\bar{c}_a$ decreases, the range of c_a increases. For instance, at $\bar{c}_a = 0.16$ we find that the maximal value of c_a is more than double the minimal value. At this and other intermediate values of $\bar{c}_a$, the concentration field in the central region of the cavity has a linear (in the horizontal direction) profile, similar to the temperature field,

$$c_a = \varsigma x + \hat{c}_a(z), \qquad (27)$$

were $\varsigma = \partial_x c_{a,i}$ is the interfacial concentration gradient and $\hat{c}_a(z)$ is the vertical concentration profile. The concentration field (27) can be obtained directly from the analytical solution for the density of vapor in the SUF regime [17]

$$\rho_v = \varrho x + \hat{\rho}_v(z) \qquad (28)$$

and the equation of state (4) which yields $c_a = 1 - \rho_v \bar{R}_v T / p_g$. The concentration gradient ς can be related not only to the horizontal density gradient ϱ, but also to the interfacial temperature gradient via the Clausius-Clapeyron equation

$$\varsigma = -\frac{\mathcal{L}(1 - c_a)}{\bar{R}_v T_s^2}\tau \approx -\frac{\mathcal{L}(1 - \bar{c}_a)}{\bar{R}_v T_0^2}\tau, \qquad (29)$$

where we used the observation that the interfacial temperature T_i is essentially equal to the saturation temperature T_s in the problem considered here [18]. The relation (29) is more general and holds for all the regimes, not just SUF.

For $\bar{c}_a \lesssim 0.08$ the horizontal concentration gradient ς is not constant and its magnitude decreases with x, while the air concentration at the hot end wall reduces to a small fraction of $\bar{c}_a$.

At the same time, the vertical concentration profile $\hat{c}_a(z)$ becomes essentially flat in the central portion of the cavity.

3.1.4. Flow regimes

The flow regimes found in the numerics for different ΔT and $\bar{c}_a$ are summarized and compared with the experimental observations of Li *et al.* [2] in Fig. 5. Instead on the dimensional parameter ΔT, the results are presented in terms of the related nondimensional parameter – the interfacial Marangoni number

$$Ma_i \equiv \frac{\gamma d_l^2}{\mu_l \alpha_l}\bar{\tau}, \qquad (30)$$

where $\bar{\tau}$ is the spatial average of the interfacial temperature gradient τ. Overall, the two sets of results are found to be in good agreement, which suggests that the model properly captures the important physical processes. The flow fields shown in Fig. 2 illustrate all the qualitatively different regimes except for partial multicellular flow (PMC) which features multiple convection rolls that do not extend all the way to the cold end wall. While this regime, intermediate between SUF and SMC [2], is expected to be found for $\Delta T = 10$ K at intermediate values of $\bar{c}_a$, our model based on a dilute approximation is not expected to produce accurate predictions when the concentrations of air and vapor are comparable. We do, however, find PMC states at higher $\bar{c}_a$ and lower ΔT, as Fig. 5 indicates.

In fact, for $\bar{c}_a \geq 0.85$ we find all four flow regimes, from SUF at low ΔT, to OMC at high ΔT. Both experiments and numerics show that a reduction in the concentration of noncondensables increases the threshold (critical Ma_i) for transition between different flow regimes. As a result, not all of the four flow regimes are found at lower $\bar{c}_a$. For instance, at $\bar{c}_a \leq 0.16$ and $\Delta T \leq 30$ K we only find SUF in the numerics. In the experiment only SUF and PMC states are found at $\bar{c}_a = 0.14$, with the latter requiring $\Delta T \gtrsim 11$ K.

At atmospheric conditions the thresholds for transitions from SUF to PMC ($Ma_i \approx 390$) and from SMC to OMC ($Ma_i \approx 780$) are very similar in the experiment and numerics, however the transition from PMC to SMC in the numerics (at $Ma_i \approx 600$) is delayed compared with the experiment (where it happens at $Ma_i \approx 430$). One potential reason for this discrepancy is the assumption of the model that condensation does not occurs on the cold end wall. In the experiment a significant fraction of the vapor likely condenses on the cold end wall, forming a thin film that drains towards the liquid layer. This can noticeably enhance condensation at all $\bar{c}_a$. As a result, for instance, the same values of Ma_i can correspond to different ΔT in the experiment and numerics.

The changes in the structure of the flow that we find at a fixed $\Delta T = 10$ K as $\bar{c}_a$ increases are qualitatively similar to the changes found at atmospheric conditions ($\bar{c}_a = 0.96$) as ΔT increases [2, 17]. Hence, it seems natural to expect that the same physical mechanism is responsible for destabilization of the uniform return flow found in the SUF regime in both cases. In order to better understand the structure and stability of the flow as a function of ΔT and $\bar{c}_a$, it is helpful to study the interfacial profiles of the velocity, temperature, and concentration

fields, as well as the mass flux J describing the intensity of phase change.

3.2. Solutions at the interface

3.2.1. The temperature and velocity profiles

Let us look at the interfacial temperature T_i first. The temperature profiles for different $\bar{c}_a$ (and fixed $\Delta T = 10$ K) are shown in Fig. 6(a). The most significant feature in all the cases is a nearly linear slope of T_i across almost the entire interface, with significant deviations only near the end walls (in the regions where thermal boundary layers form in the liquid). At intermediate values of $\bar{c}_a$ the temperature gradient τ outside the boundary layers is constant to a very good accuracy (cf. Fig. 6(b)). For $\bar{c}_a \gtrsim 0.85$ the temperature gradient exhibits spatial modulation about the average value $\bar{\tau}$ with the periodicity set by the wavelength λ of the convective structure. For $\bar{c}_a \lesssim 0.08$, on the other hand, the gradient τ slowly (and monotonically) decreases with x (we will return to this in Section 3.2.3).

Although at atmospheric pressure $\bar{\tau}$ is comparable to the imposed temperature gradient $\Delta T/L$, as the concentration of air decreases, $\bar{\tau}$ also decreases and in the absence of air, the interfacial temperature becomes essentially constant, with $\bar{\tau}$ decreasing by three orders of magnitude, compared with the values found at atmospheric conditions at the same ΔT [17]. We will discuss the dependence of $\bar{\tau}$ on $\bar{c}_a$ in more detail at the end of this section, but next we turn our attention to the interfacial flow velocity u_i.

The interfacial velocity profiles for different $\bar{c}_a$ are shown in Fig. 7 and can be easily understood with the help of the analytical solution for a steady return flow in an unbounded liquid layer driven by a constant temperature gradient $\bar{\tau}$ [36, 17]. At the interface this solution gives

$$u_i = u_T + u_B = \frac{1}{4}\frac{\nu_l}{d_l}\frac{Ma_i}{Pr} + \frac{1}{48}\frac{\nu_l}{d_l}\frac{Ra}{Pr}, \tag{31}$$

where u_T and u_B are the contributions of thermocapillarity and buoyancy, respectively. For an unbounded liquid layer u_B is characterized by an "interfacial" Rayleigh number $Ra = Bo_D Ma_i$, where

$$Bo_D \equiv \frac{\rho_l g \beta_l d_l^2}{\gamma} \tag{32}$$

is the dynamic Bond number. For a bounded liquid layer we should instead use the "laboratory" Rayleigh number [18]

$$Ra_L \equiv \frac{g\beta_l d_l^4}{\nu_l \alpha_l}\frac{\Delta T}{L}. \tag{33}$$

The relative strength of buoyancy and thermocapillarity is therefore described by the ratio of the two components,

$$\frac{u_B}{u_T} = \frac{1}{12}\frac{\Delta T}{L\bar{\tau}}Bo_D, \tag{34}$$

which suggests that thermocapillarity is the dominant force when $\bar{\tau} > \tau^*$, where

$$\tau^* = \frac{Bo_D}{12}\frac{\Delta T}{L} \approx 0.06\frac{\Delta T}{L} \tag{35}$$
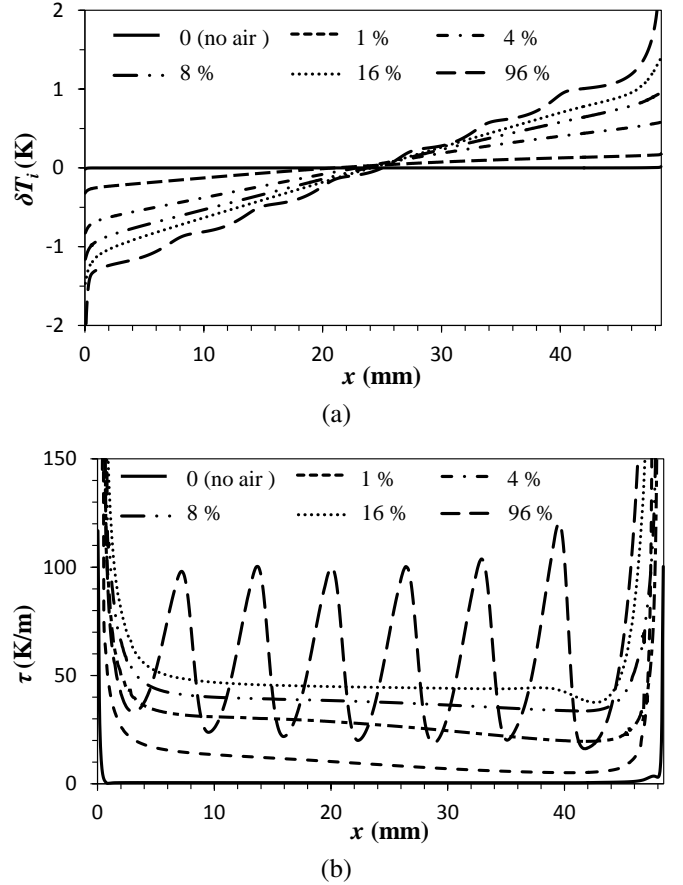

(a)

(b)

Figure 6: Interfacial temperature profile (a) and the interfacial temperature gradient $\tau = \partial_x T_i$ (b) for different average concentrations of air and $\Delta T = 10$ K. To amplify the variation of T_i in the central region of the cavity we plotted the variation $\delta T_i = T_i - \langle T_i \rangle_x$ about the average and truncated the y-axis in (a).

for the parameters considered here.

As Fig. 6(b) shows, $\bar{\tau}$ changes relatively little as $\bar{c}_a$ decreases from 0.96 to 0.16 and its magnitude remains comparable to (about a quarter of) $\Delta T/L$. Hence, the interfacial flow velocity is determined by the interfacial temperature gradient, $u_i \approx u_T \propto \tau$, even locally. In particular, u_i exhibits spatial modulation reflecting spatial modulation in τ at higher $\bar{c}_a$. As $\bar{c}_a$ is decreased below about 0.01, $\bar{\tau}$ becomes less that τ^*, so buoyancy force becomes dominant and the analytical solution (31) completely breaks down. In this limit the flow velocity is controlled by two large convection rolls driven by buoyancy, with pronounced maxima near the two end walls. The flow at $\bar{c}_a \lesssim 0.01$ is similar to that found under pure vapor [18] and corresponds to the limit of infinite Bo_D at atmospheric conditions (when buoyancy dominates over thermocapillarity). Hence, the effect of reducing $\bar{c}_a$ from the atmospheric value 0.96 to that corresponding to pure vapor ($\bar{c}_a = 0$) is analogous to increasing the dynamic Bond number from its reference value ($Bo_D = 0.69$ in this study) to infinity.

3.2.2. Phase change

While the concentration of noncondensable affects the velocity profile only indirectly, its effect on the phase change at the
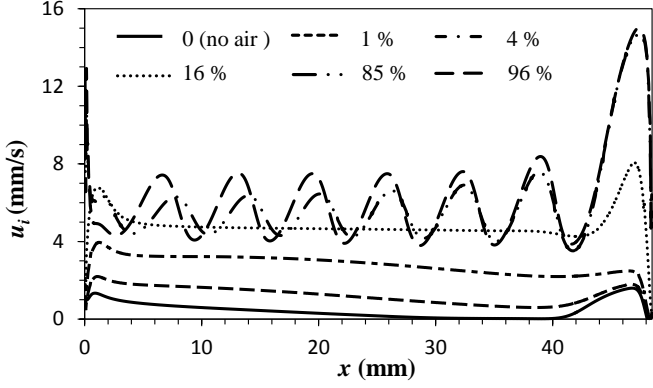
Figure 7: Interfacial velocity for different average concentrations of air and $\Delta T = 10$ K.
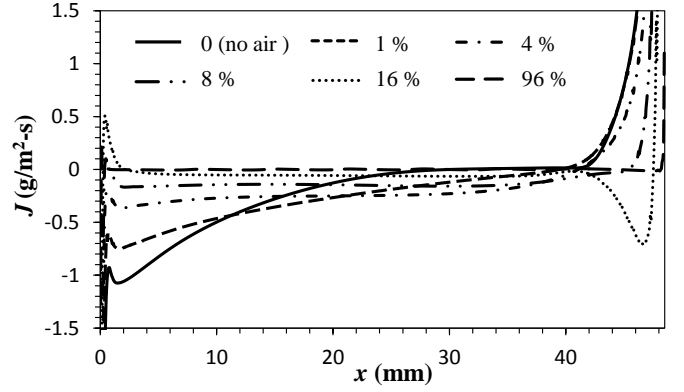

Figure 8: Mass flux due to phase change at the interface at different average concentrations of air and $\Delta T = 10$ K, with truncated y-axis.
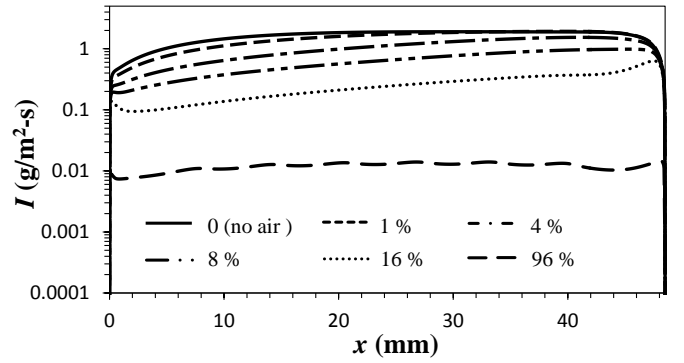

Figure 9: Integrated mass flux I at different average concentrations of air and $\Delta T = 10$ K.

interface is not only direct, but also rather dramatic. The mass flux distribution along the interface which characterizes the intensity of phase change is shown in Fig. 8. At atmospheric conditions ($\bar{c}_a = 0.96$) phase change is negligible along almost the entire interface, as transport of the vapor away from, or towards, the interface is severely restricted by diffusion through air. The phase change is only non-negligible very near the contact lines, with the liquid evaporating near the hot end wall ($J > 0$) and the vapor condensing near the cold wall ($J < 0$).

As expected, decreasing the air concentration enhances the phase change near the end walls. However, we find also significant phase change along the entire interface for $\bar{c}_a \gtrsim 0.16$. In particular, at $\bar{c}_a = 0.16$ we find a wide region near the hot end wall where $J < 0$, i.e., the vapor condenses and narrower region with $J > 0$ near the cold end wall where the liquid evaporates. This somewhat paradoxical result is due to advection, as shown in our previous work [17].

As the concentration of air is reduced further, the region of condensation expands and eventually (for $\bar{c}_a \lesssim 0.04$) extends to cover about 4/5 of the entire interface. Although the maximal values of J are still found next to the end walls (phase change is most intense in the contact line regions at all $\bar{c}_a$), phase change along the rest of the liquid-vapor interface becomes non-negligible. As $\bar{c}_a \to 0$, the mass flux J smoothly approaches the profile found in the limit of pure vapor. Similarly, the fluid flow and temperature fields, both in the bulk and at the interface, smoothly approach those found previously for pure vapor [18].

Our results for low $\bar{c}_a$ have serious implications for modeling heat pipes, which typically assume that phase change takes place only in the "evaporator" and the "condenser" regions separated by an "adiabatic" section where phase change is negligible and the temperature varies linearly [37, 38, 39]. Although the liquid flow in our model is not representative of heat pipes, the temperature profile and the flow in the gas phase are, especially at low concentrations of noncondensables, so our numerical results appear to be relevant to heat pipes. In practice, noncondensables are mostly evacuated from heat pipes to enhance phase change and the associated latent heat flux. Our results suggest that in this limit there is no "adiabatic" region, since

away from the heated/cooled end walls the temperature profile is no longer linear, while phase change is non-negligible. The models of heat pipes which ignore phase change in the "adiabatic" region appear to be based on results from experiments performed under atmospheric conditions and, in all likelihood, do not accurately describe heat and mass flow at reduced pressures.

Quantifying the net amount of phase change (and the associated latent heat) requires some care as J is not a monotonic function of x for all $\bar{c}_a$. For instance, at higher $\bar{c}_a$ some of the evaporation (condensation) near the hot (cold) end wall is offset by the condensation (evaporation) just a few mm away. At lower $\bar{c}_a$ phase change is not even localized near the end walls. To account for the non-monotonic nature of $J(x)$, we will define the characteristic mass flux J_0 across a vertical cross-section of the cavity

$$J_0 = \max_x I(x), \tag{36}$$

as the maximum of the (properly normalized) net mass flux $I(x)$ along a portion of the interface between 0 and x:

$$I(x) = \frac{1}{d_g} \left| \int_0^x J \sqrt{1 + (dz/dx)^2} \, dx \right|, \tag{37}$$

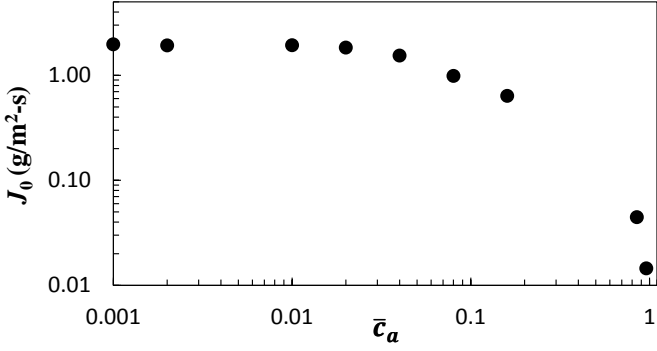where $I(L) = 0$ in steady state due to mass conservation.

9

Figure 10: Characteristic mass flux J_0 as a function of the average concentration of air at $\Delta T = 10$ K.

If phase change were localized to the contact line regions, $I(x)$ would be essentially constant in the entire "adiabatic" region and the mass flux of vapor across any vertical cross-section in that region would be equal to J_0. As Fig. 9 shows, I varies most rapidly near the contact lines where phase change is most intense for all $\bar{c}_a$. For $\bar{c}_a = 0.96$, aside from some weak modulation due to convection rolls, $I(x)$ is indeed essentially constant across most of the interface. However, for $\bar{c}_a \lesssim 0.16$, I varies rather significantly (by almost an order of magnitude!) outside of the contact line regions, which means that the "adiabatic" region disappears at reduced concentrations of noncondensables.

The dependence of the characteristic mass flux J_0 on the average concentration of noncondensables is shown in Fig. 10. As expected, J_0 is a monotonically decreasing function of $\bar{c}_a$ (noncondensables suppress phase change). J_0 does not vary noticeably for $\bar{c}_a$ below about 1%, which suggests that at low enough concentrations noncondensables essentially do not impede the flow of vapor. Increasing $\bar{c}_a$ to about 0.08 (which corresponds to 1.5% mass fraction) halves J_0, compared with the pure vapor case, at which point the adverse role of noncondensables becomes apparent, as they significantly reduce the phase change and the latent heat contribution to the heat flux. As a reference, for filmwise condensation of steam, the condensation rate is halved at air mass fraction of 0.5% [6]. At ambient conditions J_0 decreases by more than two orders of magnitude compared with the pure vapor case, which illustrates the kind of improvement in the heat flux that can be achieved by evacuating noncondensables from heat pipes and other similar passive thermal management devices.

3.2.3. The concentration profile

At high $\bar{c}_a$, phase change takes place mostly in the immediate vicinity of the contact line. Due to this, as well as the large aspect ratio of the cavity, the vapor flux from the hot side of the cavity to the cold side becomes essentially one-dimensional in the central portion of the cavity. At lower $\bar{c}_a$, phase change is non-negligible along the entire interface. However, as Fig. 4 illustrates, the concentration gradient is essentially horizontal, so the flux of vapor can again be considered one-dimensional. Even at higher $\bar{c}_a$, when the concentration gradient deviates

from horizontal, the Péclet number

$$Pe = \frac{ud_g}{D} < 1, \qquad (38)$$

so diffusion still dominates over advection. Hence, vapor transport across the cavity is controlled by diffusion in the range of ΔT considered in this study and we can ignore the variation of the mass flux of vapor with both x and z in the central portion of the cavity,

$$\mathbf{J}(x,z) \approx -J_0\hat{\mathbf{x}}, \qquad (39)$$

where

$$J_0 \approx D\partial_x\rho_v = \frac{Dp_g}{\bar{R}_v T\, p_a}\partial_x p_v, \qquad (40)$$

in agreement with the well-known result for condensation of vapor on a cold surface [40]. J_0 can be related to the average interfacial temperature gradient $\bar{\tau}$ using the Clausius-Clapeyron equation and the fact that the interfacial temperature is essentially equal to the saturation temperature [18]:

$$J_0 \approx \frac{1 - \bar{c}_a}{\bar{c}_a}\frac{\mathcal{L}Dp_g}{\bar{R}_v^2 T_0^3}\bar{\tau}. \qquad (41)$$

Note that, according to (15), the product Dp_g is independent of p_g (and hence $\bar{c}_a$), while $|T - T_0| \ll T_0$, so $\kappa = \bar{R}_v T_0/(Dp_g)$ is only a function of T_0 and can be considered a constant which has the same value in all the cases considered in this study. Furthermore, since the total pressure $p_g = p_a + p_v$ is essentially constant [18], we can rewrite (40) as

$$\kappa J_0 p_a \approx \partial_x p_v = -\partial_x p_a, \qquad (42)$$

integration of which yields the spatial profile of the partial pressure of noncondensables at the interface

$$p_a \approx \frac{\bar{c}_a}{1 - \bar{c}_a}\frac{\kappa J_0 L}{1 - e^{-\kappa J_0 L}}p_v^0 e^{-\kappa J_0 x}, \qquad (43)$$

where p_v^0 is the saturation pressure of vapor at T_0. And since $p_a/c_a = p_g = p_v^0/(1-\bar{c}_a)$, the concentration of noncondensables is given by

$$c_a \approx \bar{c}_a\frac{\kappa J_0 L}{1 - e^{-\kappa J_0 L}}e^{-\kappa J_0 x}. \qquad (44)$$

Both p_a and c_a have nonlinear profiles reflecting the accumulation of noncondensables near the cold end wall when $\kappa J_0 L \gtrsim 1$ (at low $\bar{c}_a$). As the combination $\kappa J_0 L$ decreases below unity (at high $\bar{c}_a$), the concentration profile becomes linear:

$$c_a \approx \bar{c}_a\left[1 + \kappa J_0\left(\frac{L}{2} - x\right)\right]. \qquad (45)$$

The transition between linear and exponential profiles should take place around $\kappa J_0 L = 1$, which corresponds to an intermediate value of $\bar{c}_a \approx 0.08$.

Our numerical results for the (normalized) air concentration at the interface, which are in very good agreement with the analytical result (45), are shown in Fig. 11. We find that the concentration of air has an exponential profile for $\bar{c}_a \lesssim 0.08$, with
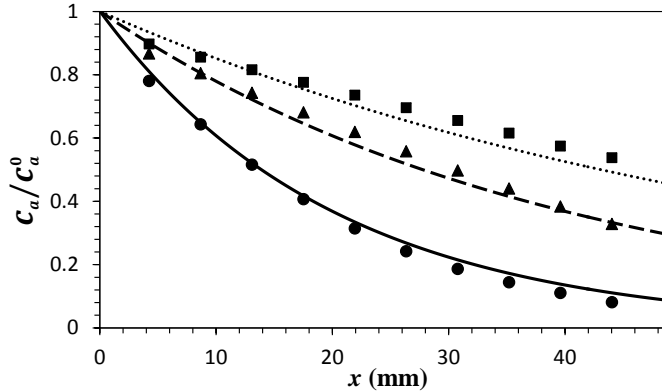
10

Figure 11: Normalized air concentration at different average concentrations of air and $\Delta T = 10$ K. Numerical and analytical results are represented by symbols and lines, respectively: $\bar{c}_a = 0.001$ (● and solid line), $\bar{c}_a = 0.08$ (▲ and dash line) and $\bar{c}_a = 0.16$ (■ and dot line).

the maximum at the cold end wall, $x = 0$. For $\bar{c}_a \gtrsim 0.16$ the concentration profile becomes essentially linear in x both along the interface and in the bulk. Since the interfacial temperature gradient τ is related to the interfacial concentration gradient ς locally via (29), for $\bar{c}_a \gtrsim 0.16$ (45) yields $\tau \approx \bar{\tau}$. For lower $\bar{c}_a$ the τ-profile also becomes exponential according to (44):

$$\frac{\tau}{\bar{\tau}} \approx \frac{c_a}{\bar{c}_a} \approx \frac{\kappa J_0 L}{1 - e^{-\kappa J_0 L}} e^{-\kappa J_0 x}, \tag{46}$$

in agreement with the numerical results shown in Fig. 6(b).

Finally, since J_0 becomes independent of $\bar{c}_a$ below about 0.02 (cf. Fig. 10), the relation (41) predicts that $\bar{\tau}$ becomes a linear function of $\bar{c}_a$. This prediction agrees with our numerical results summarized in Fig. 12 and is consistent with the result of our previous study [18], which showed that thermocapillary stresses essentially disappear when noncondensables are removed completely. In the opposite limit we find that $\bar{\tau}$ becomes almost independent of $\bar{c}_a$. In fact, $\bar{\tau}$ changes by less than 20% as $\bar{c}_a$ is decreased from 0.96 to 0.16 (which corresponds to a reduction in the partial pressure of air by over two orders of magnitude). The change in the interfacial velocity is similarly small, as Fig. 7 illustrates. This explains the puzzling experimental observation [2] that the interfacial velocity remains almost unchanged across much of the interface when the concentration of air is reduced from 0.96 to 0.14. In fact, the interfacial velocity a few mm away from the cold end wall even increases slightly as the $\bar{c}_a$ is decreased from 0.96 to around 0.16, which is also in agreement with experimental observations.

4. Summary

We have developed, implemented, and validated a comprehensive numerical model of two-phase flows of confined volatile fluids driven by an applied horizontal temperature gradient, which properly accounts for momentum, mass, and heat transport in both phases and phase change at the liquid-vapor interface. This model was used to investigate buoyancy-thermocapillary convection in a sealed cavity containing 0.65 cSt silicone oil at dynamic Bond numbers of order unity and
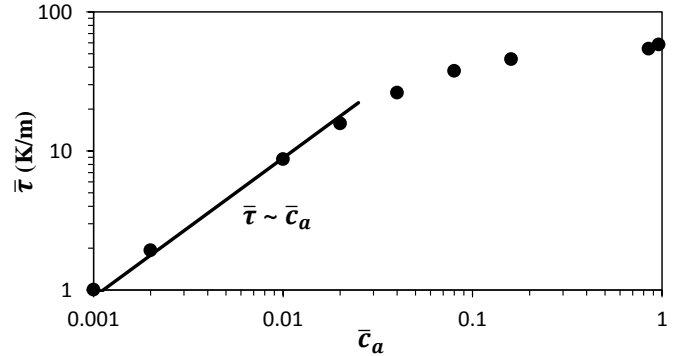

Figure 12: Average temperature gradient $\bar{\tau}$ as a function of the average concentrations of air $\bar{c}_a$ at $\Delta T = 10$ K. The solid line indicates the linear relationship predicted in the limits $\bar{c}_a \to 0$.

applied temperature gradients as high as 600 K/m. The effect of noncondensables (air) was investigated by varying their average concentration from that corresponding to ambient conditions to zero, in which case the gas phase becomes a pure vapor. The numerical results were found to interpolate between the limiting cases studied previously [17, 18]. They were also found to be in general agreement with the experimental results [2] and with the predictions of a simple analytical model of vapor transport through the gas phase.

The noncondensables were found to play a very important role in this problem. The composition of the gas phase has a crucial impact on the transport of heat, mass, and momentum. Although the fluid flow, temperature, and concentration fields generally affect each other, this interdependence can be untangled for a certain range of parameters in large-aspect-ratio cavities. Specifically, for $Pe < 1$ the transport of vapor through the gas layer is dominated by diffusion and the relative concentration of the vapor and noncondensables can be computed analytically. The concentration field profile then determines the interfacial temperature profile which, in turn, determines the interfacial velocity profile and the flow fields in both the liquid and the gas layer for $Bo_D = O(1)$.

In particular, we find that the linear temperature profile that is often assumed in the transport models is merely a limiting case of a more general, exponential profile. When the gas phase is dominated by noncondensables, the characteristic length scale on which the concentration and temperature gradients vary diverges and the exponential profiles become linear. When the vapor dominates, its flow sweeps the air towards the cold end wall, increasing the concentration and its gradient at the cold end and decreasing them at the hot end of the cavity. The resulting concentration profile in this limit deviates noticeably from linear and so does the temperature profile.

The interfacial temperature gradient differs substantially from the applied temperature gradient. It is quite sensitive to the composition of the gas phase when the concentration of noncondensables is low (below 2% or so), but becomes essentially independent of said composition at higher concentrations (above 10% or so). As a result, the speed and spatial profile of the base flow remain essentially unchanged as the partial pres-

sure of air inside the cavity is reduced from 97 kPa to around 0.75 kPa (and the total pressure – from 101 kPa to 5 kPa). Although this numerical result is consistent with the available experimental data [2], it remains somewhat counter-intuitive. In order to fully describe the thermocapillary stresses that control the flow, a more comprehensive model is needed that would allow computation of the characteristic mass flux J_0 from first principles.

While the noncondensables have a relatively weak effect on the base flow, they strongly affect its stability. As the concentration of noncondensables is decreased, the flow stability is enhanced, with critical Marangoni numbers for transitions between different flow regimes increasing rather substantially. In fact, at sufficiently low concentrations of noncondensables flow transitions disappear completely, with steady unicellular flow observed for all applied temperature gradients studied here. As we observed previously, a decrease in the concentration of noncondensables has an affect similar to that due to a decrease in the applied temperature gradient.

Qualitatively this effect can be understood rather easily. The instability leading to the formation of convection rolls is analogous to the Marangoni instability in that it is driven by the variation of the surface stresses caused by the variation in the interfacial temperature. The interfacial temperature is controlled by the local composition of the gas phase. Hence, decreasing the concentration of noncondensables increases the dissipation due to the enhanced diffusion of the vapor, reducing the variation of the concentration and interfacial temperature about the average profile corresponding to the base flow and thereby suppressing the instability.

Although the geometry investigated here is at best qualitatively similar to that of a heat pipe, some of our general results appear to be relevant for two-phase cooling technologies more broadly. In particular, we find that evacuating noncondensables from sealed cavities can significantly enhance phase change (by more than two orders of magnitude for the dimensions and working liquid considered here), although the benefit of reducing the concentration of noncondensables below about 1% is rather small. At such low concentrations significant fraction of phase change occurs away from the heated/cooled regions, so no "adiabatic" regions form where phase change can be neglected. Finally, vapor transport in the gas phase plays a crucially important role in determining the transport of both heat and mass (in the liquid phase), which opens up the possibility of constructing first-principles transport models using the intuition gleaned from numerical studies.

Acknowledgements

References

[1] A. Faghri, Heat Pipe Science And Technology, Taylor & Francis Group, Boca Raton, 1995.

[2] Y. Li, R. O. Grigoriev, M. Yoda, Experimental study of the effect of noncondensables on buoyancy-thermocapillary convection in a volatile low-viscosity silicone oil, Phys. Fluids 26 (2014) 122112.

[3] G. Peterson, An Introduction to Heat Pipes: Modeling, Testing, and Applications, Wiley-Interscience, New York, 1994.

[4] J. Collier, J. Thome, Convective Boiling and Condensation, Clarendon Press, Oxford, 1996.

[5] W. Nusselt, Die Oberflachenkondensation des Wasserdampfes, Zeitschrift des Vereins Deutscher Ingenieure 60 (1916) 569.

[6] W. Minkowycz, E. Sparrow, Condensation Heat Transfer in the Presence of Noncondensables, Interfacial Resistance, Superheating, Variable Properties, and Diffusion, Int. J. Heat Mass Trans. 9 (1966) 1125.

[7] E. Sparrow, W. Minkowycz, M. Saddy, Forced Convection Condensation in the Presence of Noncondensables and Interfacial Resistance, Int. J. Heat Mass Trans. 10 (1967) 1829.

[8] D. Villers, J. K. Platten, Coupled buoyancy and Marangoni convection in acetone: experiments and comparison with numerical simulations, J. Fluid Mech. 234 (1992) 487–510.

[9] H. Ben Hadid, B. Roux, Buoyancy- and thermocapillary-driven flows in differentially heated cavities for low-Prandtl-number fluids, J. Fluid Mech. 235 (1992) 1–36.

[10] M. Mundrane, A. Zebib, Oscillatory buoyant thermocapillary flow, Phys. Fluids 6 (10) (1994) 3294–3306.

[11] X. Lu, L. Zhuang, Numerical study of buoyancy- and thermocapillary-driven flows in a cavity, Acta Mech Sinica (English Series) 14 (2) (1998) 130–138.

[12] V. M. Shevtsova, A. A. Nepomnyashchy, J. C. Legros, Thermocapillary-buoyancy convection in a shallow cavity heated from the side, Phys. Rev. E 67 (2003) 066308.

[13] C. De Saedeleer, A. Garcimartín, G. Chavepeyer, J. K. Platten, G. Lebon, The instability of a liquid layer heated from the side when the upper surface is open to air, Phys. Fluids 8 (3) (1996) 670–676.

[14] A. Garcimartín, N. Mukolobwiez, F. Daviaud, Origin of waves in surface-tension-driven convection, Phys. Rev. E 56 (1997) 1699–1705.

[15] R. J. Riley, G. P. Neitzel, Instability of thermocapillarybuoyancy convection in shallow layers. Part 1. Characterization of steady and oscillatory instabilities, J. Fluid Mech. 359 (1998) 143–164.

[16] T. Qin, R. O. Grigoriev, Convection, evaporation, and condensation of simple and binary fluids in confined geometries, in: Proc. of the 3rd Micro/Nanoscale Heat & Mass Transfer International Conference, paper MNHMT2012–75266, 2012.

[17] T. Qin, Ž. Tuković, R. O. Grigoriev, Buoyancy-thermocapillary convection of volatile fluids under atmospheric conditions, Int. J Heat Mass Transf. 75 (2014) 284–301.

[18] T. Qin, Ž. Tuković, R. O. Grigoriev, Buoyancy-thermocapillary Convection of Volatile Fluids under their Vapors, Int. J Heat Mass Transf. 80 (2015) 38–49.

[19] J. Zhang, S. J. Watson, H. Wong, Fluid Flow and Heat Transfer in a Dual-Wet Micro Heat Pipe, J. Fluid Mech. 589 (2007) 1–31.

[20] G. V. Kuznetzov, A. E. Sitnikov, Numerical Modeling of Heat and Mass Transfer in a Low-Temperature Heat Pipe, J. Eng. Phys. Thermophys. 75 (2002) 840–848.

[21] T. Kaya, J. Goldak, Three-Dimensional Numerical Analysis of Heat and Mass Transfer in Heat Pipes, Heat Mass Transfer 43 (2007) 775–785.

[22] K. Kafeel, A. Turan, Axi-symmetric Simulation of a Two Phase Vertical Thermosyphon using Eulerian Two-Fluid Methodology, Heat Mass Transfer 49 (2013) 1089–1099.

[23] B. Fadhl, L. C. Wrobel, H. Jouhara, Numerical Modelling of the Temperature Distribution in a Two-Phase Closed Thermosyphon, Applied Thermal Engineering 60 (2013) 122–131.

[24] T. Qin, R. O. Grigoriev, The effect of noncondensables on buoyancy-thermocapillary convection in confined and volatile fluids, in: Proc. of 11th AIAA/ASME Joint Thermophysics and Heat Transfer Conference, AIAA Aviation and Aeronautics Forum and Exposition, paper AIAA2014–1898558, 2014.

[25] S. Chapman, T. Cowling, The mathematical theory of non-uniform gases: an account of the kinetic theory of viscosity, thermal conduction, and diffusion in gases, Cambridge University Press, Cambridge, 1990.

[26] B. B. Hamel, Two-Fluid Hydrodynamic Equations for a Neutral, Disparate-Mass, Binary Mixture, Phys. Fluids 9 (1966) 12.

[27] R. W. Schrage, A Theoretical Study of Interface Mass Transfer, Columbia University Press, New York, 1953.

[28] J. Klentzman, V. S. Ajaev, The effect of evaporation on fingering instabilities, Phys. Fluids 21 (2009) 122101.

[29] G. Wyllie, Evaporation and surface structure of liquids, Proc. Royal Soc. London 197 (1949) 383–395.

[30] R. Rudolf, M. Itoh, Y. Viisanen, P. Wagner, Sticking probabilities for condensation of polar and nonpolar vapor molecules, in: N. Fukuta, P. E. Wagner (Eds.), Nucleation and Atmospheric Aerosols, A. Deepak Publishing, Hampton, 165–168, 1992.

[31] H. Wang, Z. Pan, S. V. Garimella, Numerical investigation of heat and mass transfer from an evaporating meniscus in a heated open groove, Int. J. Heat Mass Transfer 54 (2011) 30153023.

[32] http://www.openfoam.com, ????

[33] C. L. Yaws, Yaws' Handbook of Thermodynamic and Physical Properties of Chemical Compounds (Electronic Edition): physical, thermodynamic and transport properties for 5,000 organic chemical compounds, Knovel, Norwich, 2003.

[34] C. L. Yaws, Yaws' Thermophysical Properties of Chemicals and Hydrocarbons (Electronic Edition), Knovel, Norwich, 2009.

[35] O. L. Flaningam, Vapor Pressures of Poly(dimethylsiloxane) Oligomers, J. Chem. Eng. Data 31 (1986) 266–272.

[36] R. V. Birikh, Thermocapillary convection in a horizontal layer of liquid, J. Appl. Mech. Tech. Phys. 7 (1966) 43–44.

[37] J. M. Ha, G. P. Peterson, Analytical Prediction of the Axial Dryout Point for Evaporating Liquids in Triangular Microgrooves, ASME J. Heat Transfer 116 (1994) 498–503.

[38] B. Suman, P. Kumar, An analytical model for fluid flow and heat transfer in a micro-heat pipe of polygonal shape, International Journal of Heat and Mass Transfer 48 (21-22) (2005) 4498–4509, ISSN 0017-9310.

[39] M. Markos, V. S. Ajaev, G. M. Homsy, Steady flow and evaporation of a volatile liquid in a wedge, Phys. Fluids 18 (2006) 092102.

[40] D. Kroger, W. Rohsenow, Condensation Heat Transfer in the Presence of a Noncondensable Gas, Int. J. Heat Mass Trans. 11 (1968) 15.